



The University of Bradford Institutional Repository

<http://bradscholars.brad.ac.uk>

This work is made available online in accordance with publisher policies. Please refer to the repository record for this item and our Policy Document available from the repository home page for further information.

To see the final version of this work please visit the publisher's website. Access to the published online version may require a subscription.

Link to publisher's version: <http://dx.doi.org/10.1016/j.jher.2012.12.001>

Citation: Pu JH, Shao S and Huang Y (2014) Numerical and experimental turbulence studies on shallow open channel flows. *Journal of Hydro-Environment Research*. 8(1): 9-19.

Copyright statement: © 2014 Elsevier B.V. Reproduced in accordance with the publisher's self-archiving policy. This manuscript version is made available under the [CC-BY-NC-ND 4.0 license](#).



Turbulence Studies of Shallow Open Channel Flows Using Numerical and Experimental Approaches

JAAN HUI PU, Assistant Professor, 53, Kabanbay Batyr Avenue, School of Engineering, Nazarbayev University, Astana 010000, Republic of Kazakhstan.

Email: jhpu@nu.edu.kz (author of correspondence)

SONGDONG SHAO, Senior Lecturer, School of Engineering, Design and Technology, University of Bradford, West Yorkshire BD7 1DP, United Kingdom.

Email: s.shao@bradford.ac.uk

ABSTRACT

Based on the previous studies, the shallow water equations (SWEs) model was proven to be insufficient to consider the flow turbulence due to its simplified Reynolds-averaged form. In this study, the k- ϵ model was used to improve the ability of the SWEs model to capture the flow turbulence. In terms of the numerical source terms modelling, the combined k- ϵ SWEs model was improved by a recently proposed surface gradient upwind method (SGUM) to facilitate the extra turbulent kinetic energy (TKE) source terms in the simulation. The laboratory experiments on both the smooth and rough bed flows were also conducted under the uniform and non-uniform flow conditions for the validation of the proposed numerical model. The numerical simulations were compared to the measured data in the flow velocity, TKE and power spectrum. In the power spectrum comparisons, a well-studied Kolmogorov's rule was also employed to complement both the numerical and experimental results and to demonstrate that the energy cascade trend was well-held by the investigated flows.

Keywords: k- ϵ model; laboratory experiments; power spectrum; rough bed flows; smooth bed flows; SGUM model; SWEs model; TKE

1 Introduction

The shallow water flows are of significant theoretical and practical interests and various experimental and numerical works have been carried out to address different issues involved, such as in Cheng et al. (2012), Liang et al. (2007) and Lin et al. (2011). To compensate the simplicity of shallow water numerical model to reproduce the flow turbulence, various turbulence equations have been investigated. For example, one of the most common applications of such approach is on the dam-break flows as presented in Ozmen-Cagatay and Kocaman (2010). The two common turbulence shallow water equations (SWEs) were usually based on the principles of 1) variation of the turbulent eddy viscosity, such as the turbulent energy and energy dissipation related models (Rodi 1993), and 2) variation of the Reynolds stress, such as the Reynolds stress models (RSM) (Launder et al. 1975). There are also some other models, which were derived from both the $k-\epsilon$ and RSM equations, namely the Launder and Ying (LY) model (1973). Those equations were first suggested by Launder and Ying (1973), and further tested in Shiono et al. (2003).

The flow turbulence equations that involve the Reynolds stress modelling, such as the RSM and LY equations, are more suitable to represent the highly turbulent flows, e.g. in the vegetated flows of Choi and Kang (2004) and compound channel flows of Shiono et al. (2003), where secondary currents are present. However, from the formulation of the turbulence equations, it can be observed that the RSM equations are more computationally expensive than the $k-\epsilon$ equations (refer to the full explanations of RSM concept in Shiono et al. 2003, and Choi and Kang 2004). As for the wide channel flows with less intense eddy formations, e.g. the shallow water flows, the $k-\epsilon$ equations were proven to well-represent the flow turbulence (refer to Gomez 2005 and Erpicum et al. 2009 studies of shallow water $k-\epsilon$ models under different flow conditions).

On the other hand, the use of power spectrum to indicate the mechanism of turbulence and turbulent kinetic energy (TKE) cascade system was first expressed in a universal manner by Kolmogorov (1941a, 1941b, 1941c). In his works, the power spectrum was categorised into three ranges: the non-viscous subrange, inertial subrange, and viscous range. The non-viscous subrange is a short range, which in a relatively small experimental flume with small width, e.g. studied by Kironoto and Graf (1995), it only lasted for one decade from 0.1Hz to almost 1Hz. Under this range, all the energy is supplied by the external sources/forces, hence an almost constant energy cascade pattern can be observed.

In the inertial subrange, the energy cascade occurs in the locally isotropy condition Kolmogorov (1941a). Derived from the 2/3 law suggested by Kolmogorov (1941a) for the second moment of turbulence, he further proposed a universal slope of $-5/3$ for the power spectrum in this subrange for

the large Reynolds number (Re) flow (Kolmogorov 1941b, 1941c; Batchelor and Townsend 1949). This law of $-5/3$ slope, also called K41 scaling rule, has later been investigated by many researches and proved for its universality in different flow conditions (Nezu and Nakagawa 1993; Frisch 1995; Mordant et al. 2004; and Blanckaert and Lemmin 2006).

When the flow Reynolds number is large, the flow energy-contained eddies are larger than the dissipating eddies, and thus it causes a broader inertial subrange (Frisch 1995). Since the inertial subrange is located between the non-viscous and viscous ranges, its energy dissipation trend has a significant influence to the whole flow energy cascade system. In Kironoto and Graf (1995), the inertial subrange was found to start at about 1Hz and ends at about 10Hz for flows at their relatively small flume with 0.6m width.

In the outmost viscous range, the TKE dissipation causes a fast energy cascade and the slope value of its power spectrum is dependent on each specific flow condition. Usually it should be greater than that in the inertial subrange due to the high turbulent viscosity in this range (Tchen 1953; and Frisch 1995). More recently, the energy cascade system and the Kolmogorov's rule have been investigated and proven numerically by Aristov and Rovenskaya (2011) using a Boltzmann kinetic turbulence model; while, the mechanism of large and small scale eddies and their effects towards the energy cascade system was studied theoretically by Hunt et al. (2010).

Conclusively, the whole three-range power spectrum describes the energy cascade process begins from the flow's energy receiving (associates with its large eddies in low-frequency), and then evolves to the flow's energy dissipating (associates with its reformation into the small eddies with high frequency). Out of the three turbulence ranges, the inertial subrange has the most universal energy cascade pattern, hence in the present study, the focus were put on to investigate this subrange.

A lot of useful works have been done on the standard turbulence $k-\epsilon$ modelling with the SWEs, so in the current work we proposed a numerical $k-\epsilon$ SWEs modelling improvement by using a documented source terms treatment method into the standard 2D finite volume scheme. This improvement was done by integrating a 1D surface gradient upwind method (SGUM) as proposed by Pu et al. (2012) into the 2D $k-\epsilon$ SWEs model here as the SGUM is robust to improve the efficiency of numerical scheme that burdened by additional TKE source terms in our investigation. An experimental study on different flow conditions has also been carried out to validate the proposed modelled results. Both the numerical and experimental models were used to investigate the shallow water flows under smooth and rough bed conditions. The numerical simulations were compared to the experimental measurements in terms of the flow velocity, TKE and power spectrum. Besides, the SWEs computed

turbulence power spectrums were also compared with the Kolmogorov's (1941a, 1941b, 1941c) scaling rule in the inertial subrange, for which very limited works have been documented in the SWEs literature.

2 Numerical Models

2.1 Shallow water equations model

In this study, the SWEs model is used to couple with the turbulence k- ε model. The 2D fully conservative shallow water equations are presented in equations (1) – (3), and it is combined with the numerical flux terms from the 2D k- ε model.

$$\frac{\partial \phi}{\partial t} + \frac{\partial \phi u}{\partial x} + \frac{\partial \phi v}{\partial y} = 0 \quad (1)$$

$$\begin{aligned} \frac{\partial \phi u}{\partial t} + \frac{\partial (\phi u^2 + \phi^2 / 2)}{\partial x} + \frac{\partial \phi uv}{\partial y} - \frac{\partial}{\partial x} \left[2\nu_t \frac{\partial (\phi u)}{\partial x} - \frac{2}{3} \phi k \right] - \frac{\partial}{\partial y} \left[\nu_t \left(\frac{\partial (\phi u)}{\partial y} + \frac{\partial (\phi v)}{\partial x} \right) \right] \\ = g\phi (S_{ox} - S_{fx}) \end{aligned} \quad (2)$$

$$\begin{aligned} \frac{\partial \phi v}{\partial t} + \frac{\partial \phi uv}{\partial x} + \frac{\partial (\phi v^2 + \phi^2 / 2)}{\partial y} - \frac{\partial}{\partial x} \left[\nu_t \left(\frac{\partial (\phi u)}{\partial y} + \frac{\partial (\phi v)}{\partial x} \right) \right] - \frac{\partial}{\partial y} \left[2\nu_t \frac{\partial (\phi v)}{\partial y} - \frac{2}{3} \phi k \right] \\ = g\phi (S_{oy} - S_{fy}) \end{aligned} \quad (3)$$

In these equations, the variable ϕ refers to geopotential and is given by $\phi = g \cdot h$, where h is the water depth and g is the gravitational acceleration. u and v are the depth averaged flow velocities in streamwise and lateral-directions, respectively. k is the flow turbulent kinetic energy (TKE), and the depth-averaged turbulent viscosity ν_t is calculated as $\nu_t = C_\mu k^2 / \varepsilon$, where C_μ is the turbulence viscosity coefficient. x , y and t denote the spatial-longitudinal, spatial-transverse and temporal domains, respectively.

In equations (2) and (3), S_{ox} and S_{oy} are the bed slopes in the streamwise and lateral directions, respectively. The friction slope of the channel S_f in the same equations are given by

$$S_{fx} = \frac{n^2 u \sqrt{u^2 + v^2}}{h^{4/3}}, \text{ and } S_{fy} = \frac{n^2 v \sqrt{u^2 + v^2}}{h^{4/3}} \quad (4)$$

where n is the Manning's friction coefficient.

2.2 k - ε turbulence model

The 2D k - ε equations to be coupled with the SWEs model used in this study can be represented by (Younus and Chaudhry 1994; Cea et al. 2007; and Pu 2008)

$$\frac{\partial \phi k}{\partial t} + \frac{\partial \phi u k}{\partial x} + \frac{\partial \phi v k}{\partial y} - \frac{\partial}{\partial x} \left[\frac{v_t}{\sigma_k} \cdot \frac{\partial(\phi k)}{\partial x} \right] - \frac{\partial}{\partial y} \left[\frac{v_t}{\sigma_k} \cdot \frac{\partial(\phi k)}{\partial y} \right] = g \cdot R_h + g \cdot R_k - \phi \varepsilon \quad (5)$$

$$\frac{\partial \phi \varepsilon}{\partial t} + \frac{\partial \phi u \varepsilon}{\partial x} + \frac{\partial \phi v \varepsilon}{\partial y} - \frac{\partial}{\partial x} \left[\frac{v_t}{\sigma_\varepsilon} \cdot \frac{\partial(\phi \varepsilon)}{\partial x} \right] - \frac{\partial}{\partial y} \left[\frac{v_t}{\sigma_\varepsilon} \cdot \frac{\partial(\phi \varepsilon)}{\partial y} \right] = \frac{\varepsilon}{k} (g \cdot C_1 \cdot R_h - C_2 \cdot \phi \varepsilon) + g \cdot R_\varepsilon \quad (6)$$

where ε is the flow TKE dissipation rate. Each of the parameter R_h , R_k , and R_ε in equations (5) and (6) can be represented as

$$R_h = \frac{v_t}{z} \left\{ 2 \left[\frac{\partial(hu)}{\partial x} \right]^2 + 2 \left[\frac{\partial(hv)}{\partial y} \right]^2 + \left[\frac{\partial(hu)}{\partial y} + \frac{\partial(hv)}{\partial x} \right]^2 \right\}, R_k = \frac{n^2 g}{h^3} (u^2 + v^2)^{\frac{3}{2}}, \text{ and}$$

$$R_\varepsilon = \frac{C_2 C_\mu n^{\frac{5}{2}} g^{\frac{5}{4}} (u^2 + v^2)^2}{h^{\frac{17}{12}}} \quad (7)$$

The turbulence parameters used in equations (5) – (7) are $C_\mu = 0.090$, $C_1 = 1.432$, $C_2 = 1.913$, $\sigma_k = 0.990$, and $\sigma_\varepsilon = 1.290$ (for a detailed study of the turbulence parameters, refer to Pu 2008).

In Table 1, a comparison of C_μ , C_1 , C_2 , σ_k and σ_ε constants used in the k - ε equations (5) – (7) and those found from the previous studies is presented. From the table, it can be observed that C_μ remains unchanged in all the tested conditions (in the present study as well as all other different reported studies). In the applications where there was a strong influence of secondary currents such as in the compound channel flow investigated by Shiono et al. (2003), the σ_k and σ_ε constants showed significant difference in comparison to the other studies, even though small variations were also observed in the present study and in Gomez (2005). However, other constants in Shiono et al. (2003) remained almost the same as other studies. It shows that the strong secondary flows existed in a channel will mainly affect the diffusion terms of the k - ε equations. In the weak secondary current flows, e.g. the vegetated flow investigated in Choi and Kang (2004) and the flow over a shallow trench investigated in Christian and Corney (2004), the k - ε equations constants remained unchanged as compared to most of the other studies. In the pipe turbulent flow studies by Zhao and Ghidaoui (2006), it can be seen that significant differences occurred in the constants C_1 and C_2 , where C_1 was reduced from the conventional values suggested by the others and C_2 showed a non-constant behavior. This is

an indication that in a non-shallow pipe flow, the production term in the energy dissipation equation is reduced and its dissipation term varies with the depth position.

3 Numerical Schemes

The numerical flux term in this study was discretized using a Godunov-type Hancock scheme. This scheme was upgraded by a two-stage predictor-corrector time-stepping concept. The Harten Lax van Leer-contact (HLLC) approximate Riemann solver was used to couple with the Godunov-type Hancock scheme for the Riemann data reconstruction process. The slope limiter method was used in the HLLC solver to ensure the space discretization scheme satisfying the flux-limiting property. The source term of the proposed numerical scheme was modelled by a surface gradient upwind method (SGUM) as proposed by Pu et al. (2012). By defining equations (1) – (3) and (5) – (6) into a single vector operation, we will get

$$\frac{\partial \mathbf{U}}{\partial t} + \nabla \cdot \mathbf{F} = \mathbf{S} \quad (8)$$

where

$$\mathbf{U} = \begin{bmatrix} \phi \\ \phi u \\ \phi v \\ \phi k \\ \phi \varepsilon \end{bmatrix}, \mathbf{F} = \begin{bmatrix} \phi Q \\ \phi u Q + \frac{\phi}{2} \left(\phi + \frac{4}{3} k \right) - 2v_t \cdot \left(\nabla_x \cdot (\phi Q) + \nabla_y \cdot \left(\frac{\phi u}{2} \right) \right) \\ \phi v Q + \frac{\phi}{2} \left(\phi + \frac{4}{3} k \right) - 2v_t \cdot \left(\nabla_y \cdot (\phi Q) + \nabla_x \cdot \left(\frac{\phi v}{2} \right) \right) \\ \frac{v_t}{\sigma_k} \cdot \nabla \cdot (\phi k) \\ \frac{v_t}{\sigma_\varepsilon} \cdot \nabla \cdot (\phi \varepsilon) \end{bmatrix}, \mathbf{S} = \begin{bmatrix} 0 \\ g\phi(S_{ox} - S_{fx}) \\ g\phi(S_{oy} - S_{fy}) \\ g \cdot P_h + g \cdot P_k - \phi \varepsilon \\ \frac{\varepsilon}{k} (g \cdot C_1 \cdot P_h - C_2 \cdot \phi \varepsilon) + g \cdot P_\varepsilon \end{bmatrix} \quad (9)$$

In equations (8) and (9), \mathbf{U} , \mathbf{F} and \mathbf{S} represent vector forms for the flow conserved variables, numerical flux and source terms, respectively; Q is the resultant velocity defined by $Q = \sqrt{u^2 + v^2}$; and ∇ is the gradient operator that can be expressed by $\nabla = \nabla_x + \nabla_y$, where $\nabla_x = \mathbf{i} \cdot \partial / \partial x$ and $\nabla_y = \mathbf{j} \cdot \partial / \partial y$. \mathbf{i} and \mathbf{j} are the unit vectors in streamwise and lateral directions, respectively.

3.1 Harten Lax van Leer-Contact (HLLC) Approximate Riemann Solver

In this study, the HLLC approximate Riemann solver used was suggested in Toro (1999) and has been further tested in Hu et al. (2006). The HLLC numerical flux is determined by

$$\mathbf{F}^{hllc} = \begin{cases} \mathbf{F}_L & \text{for } 0 \leq s_L \\ \mathbf{F}_L^* = \mathbf{F}_L + s_L (\mathbf{U}_L^* - \mathbf{U}_L) & \text{for } s_L \leq 0 \leq s_* \\ \mathbf{F}_R^* = \mathbf{F}_R + s_R (\mathbf{U}_R^* - \mathbf{U}_R) & \text{for } s_* \leq 0 \leq s_R \\ \mathbf{F}_R & \text{for } s_R \leq 0 \end{cases} \quad (10)$$

and

$$\mathbf{U}_D^* = \left(\frac{s_D - u_D}{s_D - s_*} \right) \mathbf{U}^* \quad (11)$$

Subscripts L and R represent the left and right regions of the solution cell, respectively; and superscript $*$ represents the star region that separates the left and right regions. In HLLC solver, an extra wave speed s_* is employed in the star region for updating the numerical flux. The subscript D in equation (11) represents the direction of the parameters (left L or right R). The wave speeds in equations (10) and (11) are given by:

$$\begin{aligned} s_L &= \min[u_L - c_L, u_* - c_*] \\ s_* &= \frac{(u_L + u_R)}{2} + c_L - c_R = u_* \\ s_R &= \min[u_R + c_R, u_* + c_*] \end{aligned} \quad (12)$$

where c is the wave celerity ($c = \sqrt{gh}$), and at the $*$ region, c^* is estimated as

$$c^* = \frac{(c_L + c_R)}{2} + \frac{(u_L - u_R)}{4} \quad (13)$$

In the shock capturing process, as utilised by the HLLC solver, the “dry” water wave front has to be resolved before obtaining a stable algorithm. In this study, further criteria as suggested by Toro (1999) are included to compute the water wave front condition on the left and right “dry” sides as follows

$$\text{Left “Dry” Side Criteria: } s_L = u_R - 2c_R, s_* = s_L, \text{ and } s_R = u_R + c_R \quad (14)$$

$$\text{Right “Dry” Side Criteria: } s_R = u_L + 2c_L, s_* = s_R, \text{ and } s_L = u_L - c_L \quad (15)$$

3.2 Monotone Upwind–Hancock Scheme

In this study, a robust numerical wave reconstruction scheme, Monotone Upwind Scheme for Conservative Laws (MUSCL), was used, in which both \mathbf{U}_L and \mathbf{U}_R change linearly according to their

adjacent cells (Toro 1999). The MUSCL scheme gives a second order of accuracy to the proposed FV model, and it can be expressed as

$$\mathbf{U}_{i+1/2}^L = \mathbf{U}_i - \frac{\Pi(q_i) \cdot \Delta \mathbf{U}_{i-1/2}}{2}, \text{ and, } \mathbf{U}_{i+1/2}^R = \mathbf{U}_{i+1} + \frac{\Pi(q_{i+1}) \cdot \Delta \mathbf{U}_{i+1/2}}{2} \quad (16)$$

$$\text{where } q_i = \frac{\Delta \mathbf{U}_{i+1/2}}{\Delta \mathbf{U}_{i-1/2}}, q_{i+1} = \frac{\Delta \mathbf{U}_{i+3/2}}{\Delta \mathbf{U}_{i+1/2}}, \Delta \mathbf{U}_{i+1/2} = \mathbf{U}_{i+1} - \mathbf{U}_i, \text{ and, } \Delta \mathbf{U}_{i-1/2} = \mathbf{U}_i - \mathbf{U}_{i-1} \quad (17)$$

Π is the slope limiter in equations (16) – (17); i represents the space step; and q is the gradient of successive $\Delta \mathbf{U}$. As suggested by the findings from Mingham and Causon (2000) and Hu et al. (2006), the MUSCL scheme flux in this study is determined using the van Leer limiter, where $\Pi = [q + |q|] / (1 + q)$.

A Hancock two-stage predictor-corrector scheme was utilised to update \mathbf{U} across the time domain. This approach has the advantage of being stable and could achieve second order accuracy over the time domain. The combined predictor-corrector steps are given as

$$\text{Predictor Step: } \mathbf{U}_i^{N+1/2} = \mathbf{U}_i^N - \frac{\Delta t}{2\Omega_i} (\mathbf{F}_{i+1/2}^N - \mathbf{F}_{i-1/2}^N) \quad (18)$$

$$\text{Corrector Step: } \mathbf{U}_i^{N+1} = \mathbf{U}_i^N - \frac{\Delta t}{\Omega_i} (\mathbf{F}_{i+1/2}^{N+1/2} - \mathbf{F}_{i-1/2}^{N+1/2}) \quad (19)$$

where Ω is the cell area (for the SWEs model); and N represents the time step.

The Courant-Friedrichs-Lewy stability criterion was used to ensure Δt does not exceed its maximum allowable limit, as represented by

$$\Delta t \leq C_{FL} \left[\frac{\Omega}{|Q \cdot \mathbf{s}| + c \cdot |\mathbf{s}|} \right] \quad (20)$$

where $\mathbf{s} = \mathbf{i} + \mathbf{j}$ represents the resultant normal unit vector; and C_{FL} is the Courant number, which is limited to $0 < C_{FL} \leq 1$. Smaller values of C_{FL} will give more accurate and stable results, but at an increasing computational expense.

3.3 Source Terms Scheme

An original surface gradient upwind method (SGUM) source terms treatment scheme proposed by Pu et al. (2012) was integrated in this study to describe the combined operation of \mathbf{F} and \mathbf{S} in equation

(8). This combination of \mathbf{F} and \mathbf{S} in the numerical iterations could improve the numerical accuracy to predict the flow under different conditions (Pu et al. 2012). In this work, SGUM is used to improve the numerical scheme to simulate the extra source terms from k- ϵ equations that being added into the SWEs model.

It is worth mentioning that in Pu et al. (2012) the SGUM was only applied to the 1D flow cases, but here it is adapted into the 2D shallow water model. With the application of SGUM approach, the MUSCL-Hancock scheme in equations (18) – (19) will become

$$\text{Predictor Step: } \mathbf{U}_i^{N+1/2} = \mathbf{U}_i^N - \frac{\Delta t}{2\Omega_i} (\mathbf{f}_{i+1/2}^N - \mathbf{f}_{i-1/2}^N) \quad (21)$$

$$\text{Corrector Step: } \mathbf{U}_i^{N+1} = \mathbf{U}_i^N - \frac{\Delta t}{\Omega_i} (\mathbf{f}_{i+1/2}^{N+1/2} - \mathbf{f}_{i-1/2}^{N+1/2}) \quad (22)$$

where $\mathbf{f} = \mathbf{F} - \Omega \cdot \mathbf{S}$.

Similar representation of the Hancock scheme in equations (21) and (22) has also been used by Mingham and Causon (2000), Hu et al. (2006) and many others in their 2D SWEs schemes, except that the source terms have been integrated into the scheme here by using \mathbf{f} as presented above.

3.4 Boundary and Initial Conditions

A double boundary condition is used for the proposed model, where two extra ghost-cells are utilised outside the computational space domain (Hu et al. 2006). Two kinds of boundary are considered, the open and solid boundaries. For their corresponding boundary vectors \mathbf{U}^B , it can be presented as

$$\text{Solid Boundary: } \mathbf{U}^B = [\phi \quad \phi u \quad \phi v \quad \phi k \quad \phi \epsilon]^T \quad (23)$$

$$\text{Transmissive Boundary: } \mathbf{U}^B = [\phi \quad -\phi u \quad -\phi v \quad \phi k \quad \phi \epsilon]^T \quad (24)$$

These boundary conditions are updated by using

$$\mathbf{U}_{m+1}^B = \mathbf{U}_m^B \quad (25)$$

$$\mathbf{U}_{m+2}^B = \mathbf{U}_{m-1}^B \quad (26)$$

where m is the last space step in the computational boundary excluding the ghost cells.

4 Experimental Model

To validate the numerical model, an experimental study was carried out. Figs 1 (a) – (b) present the general layout and photographical image of the hydraulic flume, which were used in the laboratory experiments. The descriptions of the experimental instrument, experimental conditions as well as rough bed flows experimental setting are discussed in details at the following sub-sections.

4.1 *Experimental Instrument*

As presented in Fig 1, a rectangular tilting flume, which is 12m long, 0.45m wide and 0.50m high, was used. The physical flume was located in the Hydraulic Laboratory at the University of Bradford, where all the experiments in this study had been carried out (Pu 2008). The upstream end of the flume is connected to the outlet pipe of a water pump, and its downstream end empties into a water tank. The water tank collects the water at downstream end before sending it to the pump to be re-circulated into the flume. The flume has glass walls and a painted-steel base. An adjustable gate is located at the downstream end of the flume to control the flow elevation in the flume. The flume is also equipped with a track parallel to the flume base for attaching the measurement trolleys, which were used as the Acoustic Doppler Velocimeter (ADV) and vernier water gauge holder. The flume slope is controlled by a mechanical screw located at the downstream of the flume, and is equipped with a calibrated scale that indicates the vertical movement of the flume. This calibrated scale allows the tilted vertical distance to be determined up to an accuracy of one millimetre. For more detailed experimental descriptions, one could refer to Pu (2008).

4.2 *Experimental Conditions*

A summary of all the hydraulic conditions in the smooth and rough bed uniform and non-uniform flow experiments are presented in Table 2. For the non-uniform flows, the velocity measurements were made at four streamwise locations (3m, 5m, 6m, and 7m from the flume inlet), whereas for the uniform flows, the measurements were made at a single 6m location of the 12m long channel. At each streamwise location, the velocity measurements were made at several vertical positions. For the smooth bed flow test, 15 – 25 vertical measuring points were used depending on the flow condition; whereas the rough bed flow test used 14 vertical measuring points (shown in Table 2). In all tests (Test 1 – 6), the velocity measurements were conducted at the ADV sampling frequency of 100Hz for 5 minutes of the sampling time.

4.3 *Rough Bed Setting*

In the experiment, the rough bed flow was created by using a non-moving layer of sediment on the channel bed. It was set up by using the water-worked concept, during which the sediment was slowly poured into the upstream of the flume, and was left to settle and form a non-moving bed layer (Cooper and Tait 2010). The feeding rate of the sediment was set as 280g/s in a 100mm uniform depth flow, which was calculated using the Meyer-Peter Muller formula. After the bed feeding, the sediment bed elevation was measured from a distance of 1.5m from the upstream end to 9.0m from the downstream end in the width of 0.05m to 0.40m [refer to Fig 2 (a)]. From Fig 2 (b), it can be observed that the width-averaged bed elevation formed quite a smooth slope of 9.0×10^{-3} with a high regression coefficient R^2 of 0.988, which means that the utilized water-worked bed has almost a uniform slope. The bed materials used was found to have the grain sizes of $d_{16} = 3.81\text{mm}$, $d_{50} = 6.62\text{mm}$ and $d_{84} = 7.94\text{mm}$. The size of d_{50} is used as the Nikuradse roughness k_s in this study. The bed material sample is shown in Fig 3 and its grain size cumulative and frequency distributions are shown in Fig 4. The density of the bed material is 2823.8kg/m^3 .

5 Results and Discussions

5.1 Flow Velocity and Turbulent Kinetic Energy (TKE)

The numerical simulations were done using the turbulence coefficients as presented in Table 1 (refer to the studies by Pu 2008) for the physical experiments as shown in Table 2. A Manning's coefficient n of 0.01 was found to be the best representation of the smooth bed experimental condition, whereas $n = 0.025$ was found to adequately represent the rough bed experimental condition. This set of n coefficients also agreed well with the Manning's coefficient study on different bed conditions in Olsen (2003).

Table 3 shows the depth-averaged streamwise velocity comparisons between the numerical simulations and experimental measurements for the smooth and rough bed flows under uniform or non-uniform flow condition (Test 1 – 6 in Table 2). Throughout the table, one can observe that for the non-uniform flows, Test 2 – 4 had the accelerating characteristic across the streamwise direction from 3m to 7m location, whereas Test 5 had the decelerating characteristic. In this study, Test 2 – 4 and Test 5 were categorised as spatial-accelerating and spatial-decelerating flows, respectively, which the similar descriptions were also used in Kironoto and Graf (1995). Observing the trend of non-uniform flows depth-averaged velocity changes across the streamwise locations, it can be seen that Test 2 and 4 showed the lowest numerical errors. However, compared to uniform flows depth-averaged velocity over smooth bed (Test1) and rough bed (Test 6) at mid-stream location, the non-uniform flows were

recording much higher numerical errors. All numerical simulations showed reasonable agreement with the experimental results with less than 5% error.

In Fig 5, the non-uniform flows (Test 2 – 5) depth-averaged numerical TKEs are presented and compared to the experimental measurements. The results were plotted against a dimensionless water depth ratio h_{dr} , which is defined as follows

$$h_{dr} = \frac{h - h_{mi}}{h_{ma} - h_{mi}} \quad (27)$$

where h_{ma} and h_{mi} are the maximum and minimum water depths across the channel, respectively. h_{dr} defines the ratio of water-head difference of a flow system. For spatial-accelerating flow, h_{dr} is decreasing from upstream to downstream in streamwise direction, whereas in spatial-decelerating flow h_{dr} is increasing. The comparison of uniform flows TKEs were excluded in this study, since their TKEs remained constant and their water-head differences were negligible.

Numerical simulations of the non-uniform flows depth-averaged TKEs at different streamwise locations matched the experimental measurements well as shown in Fig 5. The spatial-decelerating flow in Test 5 showed more energy gradient variations than all spatial-accelerating flows as shown by the greater changes of its curve across h_{dr} . This is due to the greater bed slope in the spatial-decelerating flow (compared to all spatial-accelerating flows) that created a larger pressure gradient for the flow. The greater bed slope used in Test 5 also caused a higher numerical error in the simulated TKE (with average error of 3.1%) if compared to the spatial-accelerating flows of Test 2 – 4 (with average error of 2.2%). Numerically, this greater error was caused by the larger simulated S_o source terms in the non-uniform flow, even if the source terms representation have been improved by the SGUM as proposed in Pu et al. (2012).

5.2 Power Spectrum Analysis

In this section, the Kolmogorov's (1941a, 1941b, 1941c) rule in power spectrum is first reviewed and discussed. It is then be used to compare with the proposed numerical and experimental studies finding. In the streamwise flow direction, the normalised correlation function of two continuous streamwise distance series with a short streamwise lag distance τ can be defined as (Nezu and Nakagawa 1993)

$$r(\tau) = \frac{\overline{u(x) \cdot u(x + \tau)}}{u'^2} \quad (28)$$

where r is the normalised correlation function for the flow velocity. When equation (28) undergoes a Fourier transform, its transformed real correlation (after ignoring the imaginary transform and assuming a symmetrical signal of $-\infty$ to 0 and 0 to ∞) will become (Nezu and Nakagawa 1993)

$$S_p(f_w) = \frac{2}{\pi} \int_0^{\infty} [r(\tau) \cdot \cos(f_w \cdot \tau)] d\tau \quad (29)$$

where S_p is the TKE correlated power spectrum and f_w is the wave number in streamwise direction. By adopting the von Karman spectrum theory, Heisenberg's formulae and Kolmogorov's K41 scaling rule, equation (29) becomes [as derived by Kolmogorov 1941b, 1941c; and shown at equation (2.38) at Nezu and Nakagawa 1993]

$$S_p(f_w) = \frac{C_k}{u'^2} \cdot \varepsilon^{2/3} f_w^{-5/3} \quad (30)$$

where C_k is the Kolmogorov's universal constant.

Equation (30) has been further modified by Kolmogorov's (1941b, 1941c) in his third similarity hypotheses to suggest a simplified equation of [shown at equation (2.1) at Batchelor and Townsend 1949]

$$S_p(f_w) = A_k \cdot \varepsilon^{2/3} f_w^{-5/3} \quad (31)$$

where A_k is a universal absolute constant.

In order to obtain a useful relationship of the numerical simulated parameter with the measured data in the power spectrum comparison, an derived equation from K41 scaling rule used in Nezu and Nakagawa (1993) and Hunt et al. (2010) has been utilised here as follows [shown at equation (2.39) at Nezu and Nakagawa 1993]

$$u' = \sqrt[3]{\frac{\varepsilon \cdot L_x}{k_L}} \quad (32)$$

where u' is the fluctuation of the streamwise velocity, L_x is the macroscale of turbulence, and k_L is the turbulence coefficient in which it can be represented as in equation (33). Equation (32) was used to relate the numerically calculated ε to the velocity fluctuation by using comparative parameter of L_x .

$$k_L = [2 / (\pi C_k)]^{3/2} \alpha^{5/2} \quad (33)$$

In equation (33), α is a dimensionless parameter that defined as $\alpha = L_x k_0$ in which k_0 is the initial TKE. The macroscale of turbulence L_x in equation (32) can be calculated in a compared ratio with the Kolmogorov microscale η_k as

$$\frac{L_x}{\eta_k} = 0.91 Re^{3/4} \quad (34)$$

where

$$\eta_k = \left(\frac{v_t}{\varepsilon} \right)^{1/4} \quad (35)$$

By using the relation at equation (32), u' is calculated by using the numerical computed ε before it was transformed to the frequency based power spectrum by using the fast Fourier transform (FFT) method. For the experimental data, the measured u' was also processed through the FFT operation before compared to the proposed numerical results. By using the Kolmogorov $-5/3$ theory shown in equation (31) as a comparison, the further analyses of the experimental and numerical Fourier transformed data are also carried out.

In Figs 7 – 10, the comparisons of numerically and experimentally obtained power spectra of Test 2 – 5 in Table 2 (non-uniform flow tests) were presented for the different streamwise locations, whereas the comparisons of Test 1 and 6 in Table 2 (uniform flow tests) were shown in Figs 6 and 11 for a single streamwise location at the mid-stream of the flow. The non-viscous and inertial subranges of the power spectra were clearly shown in the figures and the results were also compared to the universally agreed K41 scaling rule in the inertial subrange.

For both the non-viscous and inertial subranges, the numerical computations generally well-matched the experimental measurements in different streamwise locations of the channel (3m, 5m, 6m and 7m) (Figs 7 – 10), as well as at the single location for Test 1 and 6 (Figs 6 and 11). Particularly, the agreement in the inertial subrange showed that the numerical model reproduced the important energy cascade characteristics of the investigated flows.

When both the numerical and the experimental results were further compared to the K41 scaling rule, both of them agreed well with it in the inertial subrange. The inertial subrange energy cascade behaviour marked by the K41 scaling rule well defines a wide range of flow conditions, including the uniform and non-uniform flows as suggested by Nezu and Nakagawa (1993), hence it has also been well-represented by both the inspected uniform and non-uniform flow results here. Furthermore, the inertial subranges of all the uniform and non-uniform flow tests extended wider than 10Hz spectrum frequency, which is the suggested inertial subrange limit by Kironoto and Graf (1995) who used similar flume size as this study. This phenomenon indicates that the production of energy-contained eddies is high.

For the non-uniform flows in Test 2 – 5 (Figs 7 – 10), it can be observed that both the spatial-accelerating (Test 2 – 4) and spatial-decelerating flows (Test 5) have consistently shown very small spectra magnitude variations in different locations. This is a strong indication that the pressure

gradient difference along the channel (which is the mechanism for generating the flow accelerating and decelerating characteristics) will not have a significant effect on altering the power spectra, and this is also agreed by the non-uniform flow studies of Kironoto and Graf (1995).

6 Conclusions

A numerical model has been proposed to combine the shallow water model with k- ϵ equations to study the TKE conditions of different uniform and non-uniform flows. The model was also further improved in the source terms numerical representation by using a recently proposed SGUM approach. This combination facilitated the extra source terms generated from the k- ϵ equations into the SWEs and improved the simulation accuracy and stability of the flow energy system.

Laboratory flow experiments were conducted over the smooth and rough beds under uniform and non-uniform flow conditions to validate the proposed numerical schemes. The comparisons were accomplished in the flow velocity, TKE and power spectrum to fully investigate the ability of the numerical model to represent the energy system in different flow conditions. The results showed that the numerical model captured the experimental flow characteristics well for all the considered conditions. In addition, the simulated and measured TKE power spectra were also compared to the Kolmogorov's K41 analytical scaling rule in the flow inertial subrange and they all agreed satisfactorily with one another. All of these comparisons have proven that the proposed numerical model is capable to represent the actual flow TKE system for different bed surfaces and flow regimes.

Acknowledgements

This research work is supported by the Nazarbayev University Seed Grant, entitled “Environmental Assessment of Sediment Pollution Impact on Hydropower Plants”. The author Jaan Hui Pu would like to thank Dr Khalid Hussain and Prof Simon Tait, University of Bradford, UK for their guidance on shallow water flow modelling and flow experimental studies during his PhD.

Nomenclatures

c	wave celerity
C_{FL}	Courant number
C_k	Kolmogorov's universal constant
C_μ	turbulence viscosity coefficient
d	grain size of bed material
\mathbf{F}	numerical flux vector

f_w	wave number in x-direction
g	gravitational acceleration
h	water flow depth
h_{dr}	dimensionless water depth ratio
h_{ma}	maximum water depth across channel
h_{mi}	minimum water depth across channel
k	flow turbulent kinetic energy (TKE)
k_s	Nikuradse roughness
L_x	macroscale of turbulence
m	last computation space step
n	Manning's friction coefficient
Q	resultant velocity
r	normalised correlation function for flow velocity
s	wave speed
\mathbf{S}	source terms vector
S_f	flow friction slope
S_o	flow bed slope
S_p	power spectrum
t	time
u	depth-averaged velocity in streamwise direction
\mathbf{U}	flow conserved variables vector
v	depth-averaged velocity in lateral direction
x	longitudinal distance
y	lateral distance
∇	gradient operator
ε	energy dissipation
Ω	computation cell volume
ν_t	depth-averaged turbulent viscosity

Subscripts and Symbols

ADV	acoustic Doppler velocimeter
FFT	fast Fourier transform

HLLC	Harten Lax van Leer-contact
K41	Kolmogorov universal power spectrum rule
L	left region
R	right region
Re	Reynolds number
SGUM	surface gradient upwind method
SWEs	shallow water equations
TKE	turbulent kinetic energy
*	star region

References

- Aristov, V.V., Rovenskaya, O.I., 2011. Application of Boltzmann kinetic equation to the Eddy problems. *Comput. Fluids*. 50(1), 189-198.
- Batchelor, G.K., Townsend, A.A., 1949. The nature of turbulent motion at large wave numbers. *Proc. Roy. Soc. London Ser-A Math. Phys. Sci.* 199(1057), 238-255.
- Blanckaert, K., Lemmin, U., 2006. Means of noise reduction in acoustic turbulence measurements. *J. Hydraul. Res.* 44(1), 1-15.
- Cea, L., Puertas, J., Vazquez-Cendon, M.E., 2007. Depth average modelling of turbulent shallow water flow with wet-dry fronts. *Arch. Comput. Meth. Eng.* 14, 303-341.
- Cheng, N.S., Nguyen, H.T., Tan, S.K., Shao, S., 2012. Scaling of velocity profiles for depth-limited open channel flows over submerged rigid vegetation. *J. Hydraul. Eng.* 138(8), 673–683.
- Choi, S.U., Kang, H., 2004. Reynolds stress modeling of vegetated open-channel flows. *J. Hydraul. Res.* 42(1), 3-11.
- Christian, C.D., Corney, P.A., 2004. Three dimensional model of flow over a shallow trench. *J. Hydraul. Res.* 42(1), 71-80.
- Cooper, J.R., Tait, S.J., 2010. Spatial representative velocity measurement over water-worked gravel beds. *Water Resour. Res.* 46(W11559), 1-15.
- Epicum, S., Meile, T., Dewals, B.J., Piroton, M., Schleiss, A.J., 2009. 2D numerical flow modeling in a macro-rough channel. *Int. J. Numer. Meth. Fluids.* 61(11), 1227-1246.
- Frisch, U., 1995. *Turbulence – the legacy of A. N. Kolmogorov*, first ed. Cambridge University Press.
- Gomez, L.C., 2005. An unstructured finite volume for unsteady turbulent shallow water flow with wet-dry fronts: numerical solver and experimental validation. PhD Thesis, Universidad De La Coruna, La Coruna, Spain.

- Hu, K., Mingham, C.G., Causon, D.M., 2006. A mesh patching method for finite volume modelling of shallow water flow. *Int. J. Numer. Meth. Fluids*. 50, 1381-1404.
- Hunt, J.C.R., Eames, I., Westerweel, J., Davidson, P.A., Voropayev, S., Fernando, J., Braza, M., 2010. Thin shear layers – the key to turbulence structure? *J. Hydro-environ. Res.* 4, 75-82.
- Kironoto, B.A., Graf, W.H., 1995. Turbulence characteristics in rough non-uniform open-channel flow. *Proc. Instn. Civ. Engrs. Wat. Marit. Energy*. 112, 336-348.
- Kolmogorov, A.N., 1941a. The local structure of turbulence in incompressible viscous fluid for very large Reynolds number. *C.R. Acad. Sci. URSS*. 30, 301-305.
- Kolmogorov, A.N., 1941b. On the degeneration of isotropic turbulence in an incompressible viscous fluids. *C.R. Acad. Sci. URSS*. 31, 538-541.
- Kolmogorov, A.N., 1941c. Dissipation of energy in isotropic turbulence. *C.R. Acad. Sci. URSS*. 32, 19-21.
- Launder, B.E., Reece, G.J., Rodi, W., 1975. Progress in the development of a Reynolds-stress turbulence closure. *J. Fluid Mech.* 68, 537-566.
- Launder, B.E., Ying, W.H., 1973. Prediction of flow and heat transfer in duct of square cross section. *Proc. Instn. Mech. Eng.* 187, 455-461.
- Liang, D., Lin, B., Falconer, R. A., 2007. Simulation of rapidly varying flow using an efficient TVD-MacCormack scheme. *Int. J. Numer. Meth. Fluids*. 53, 811-826.
- Lin, P.Z., Wu, Y.N., Bai, J.L., Lin, Q.H., 2011. A numerical study of dam-break flow and sediment transport from a quake lake. *J. Earthq. Tsunami*. 5(5), 401-428.
- Mingham, C.G., Causon, D.M., 2000. Calculation of unsteady bore diffraction using a high resolution finite volume method. *J. Hydraul. Res.* 38(1), 49-56.
- Mordant, N., Leveque, E., Pinton, J.F., 2004. Experimental and numerical study of the Lagrangian dynamics of high Reynolds turbulence. *New J. Phys.* 6, 1-44.
- Nezu, I., Nakagawa, H., 1993. Turbulent open-channel flows. IAHR Monograph, A. A. Balkema, Rotterdam, the Netherlands.
- Olsen, N.R.B., 2003. *Hydroinformatics, Fluvial Hydraulics and Limnology*, third ed. The Norwegian University of Science and Technology, Norway.
- Ozmen-Cagatay, H., Kocaman, S., 2010. Dam-break flows during initial stage using SWE and RANS approaches. *J. Hydraul. Res.* 48(5), 603-611.
- Pu, J.H., 2008. Efficient finite volume numerical modelling and experimental study of 2D shallow water free surface turbulent flows. PhD Thesis, University of Bradford, Bradford, UK.

- Pu, J.H., Cheng, N.-S., Tan, S.K., Shao, S., 2012. Source terms treatment of SWEs using surface gradient upwind method. *J. Hydraul. Res.* 50(2), 145-153.
- Rodi, W., 1993. Turbulence models and their application in hydraulics. IAHR Monograph, Taylor and Francis, New York, United States of America.
- Shiono, K., Scott, C.F., Kearney, D., 2003. Predictions of solute transport in a compound channel using turbulence models. *J. Hydraul. Res.* 41(3), 247-258.
- Tchen, C.M., 1953. On the spectrum of energy in turbulent shear flow. *J. Res. Nat. Bur. Stand.* 50(1), 51-62.
- Toro, E.F., 1999. Riemann solvers and numerical methods for fluid dynamics: a practical introduction, second ed. Springer-Verlag, Berlin, Germany.
- Younus, M., Chaudhry, M.H., 1994. A depth-averaged $k-\epsilon$ turbulent model for the computation of free-surface flow. *J. Hydraul. Res.* 32(3), 415-444.
- Zhao, M., and Ghidaoui, M.S., 2006. Investigation of turbulence behaviour in pipe transient using a $k-\epsilon$ model. *J. Hydraul. Res.* 44(5), 682-692.

Table 1. k-ε model empirical constants from present study and literatures

	C_μ	C_1	C_2	σ_k	σ_ε
Present study	0.090	1.432	1.913	0.990	1.290
Shiono et al. (2003)	0.090	1.440	1.920	1.225	1.225
Choi and Kang (2004), Christian and Corney (2004), and Cotton et al. (2005)	0.090	1.440	1.920	1.000	1.300
Gomez (2005)	0.090	1.440	1.920	1.000	1.310
Zhao and Ghidaoui (2006)	0.090	1.390	$1.800f_c^\dagger$	1.000	1.300

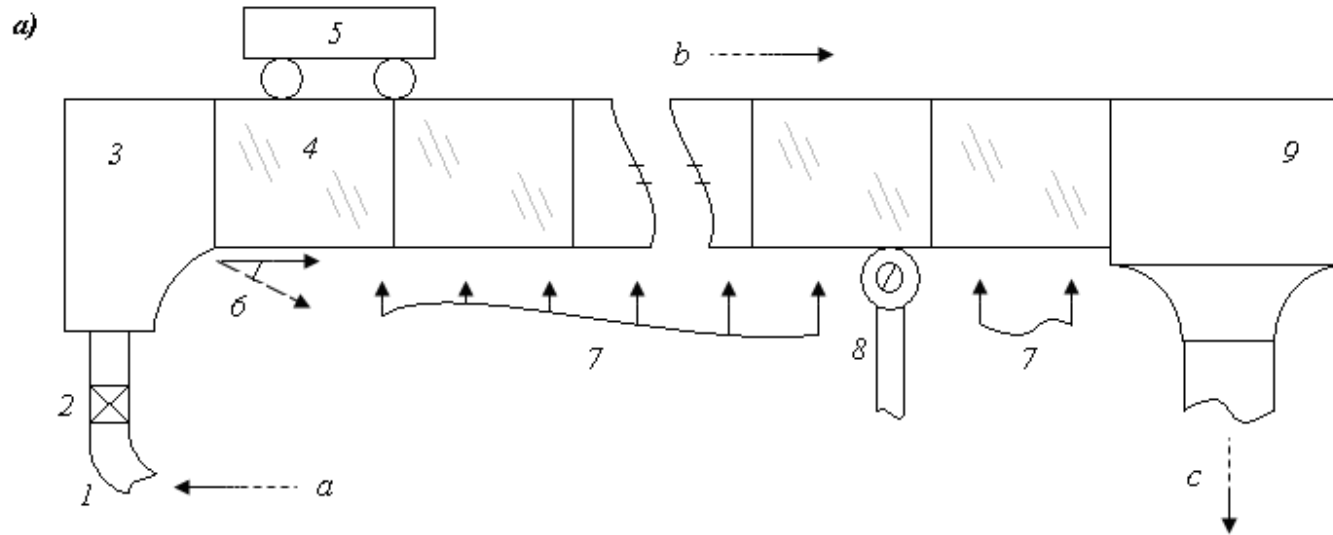
$\dagger f_c = \left\{ 1.00 - 0.22 \exp \left[- \left(R_t / 6 \right)^2 \right] \right\} R_w^2$, where
 $R_w = 1.00 - \exp \left\{ -\sqrt{R_z} / 2.30 + \left(\sqrt{R_z} / 2.30 - R_z / 8.89 \right) \left[1.00 - \exp(-R_z / 20) \right]^3 \right\}$,
 $R_t = k^2 / (v\varepsilon)$,
 $R_z = \sqrt{kz} / v$, and
 z is the height from bed to measuring point.

Table 2. Summary of experimental conditions in uniform and non-uniform flows

Test No.	Slope ($\times 10^{-3}$)	Discharge (m^3/s)	Flow Characteristics	Bed Condition	No. of Measured Point
1	1.25	0.0315	Uniform	Smooth	20
2	Flat	0.0270	Non-uniform	Smooth	20
3	Flat	0.0315	Non-uniform	Smooth	22
4	Flat	0.0360	Non-uniform	Smooth	25
5	2.50	0.0315	Non-uniform	Smooth	15–19
6	4.8	0.0405	Uniform	Rough	14

Table 3. Comparisons of experimental measurements and numerical predictions of the depth-averaged u-velocities (Test 1 – 6 in Table 2)

Test No.	Category	Depth Averaged u-Velocity (m/s)			
		3m	5m	6m	7m
1	Experimental	-	-	0.567	-
	Numerical	-	-	0.569	-
	<i>% Error</i>	-	-	0.35	-
2	Experimental	0.482	0.502	0.505	0.510
	Numerical	0.475	0.500	0.512	0.514
	<i>% Error</i>	1.45	0.40	1.39	0.78
3	Experimental	0.509	0.517	0.519	0.528
	Numerical	0.487	0.515	0.529	0.539
	<i>% Error</i>	4.32	0.39	1.93	1.89
4	Experimental	0.551	0.555	0.564	0.599
	Numerical	0.548	0.562	0.575	0.588
	<i>% Error</i>	0.54	1.26	1.95	1.84
5	Experimental	0.788	0.757	0.695	0.686
	Numerical	0.785	0.762	0.720	0.705
	<i>% Error</i>	0.38	0.66	3.60	2.77
6	Experimental	-	-	0.730	-
	Numerical	-	-	0.728	-
	<i>% Error</i>	-	-	0.27	-



Parts:

- 1 Inlet Water Pipe
- 2 Discharge Control Valve
- 3 Inlet Tank
- 4 Water Flume (Glass-Walled)
- 5 Trolley (ADV Holder)
- 6 Angle of Flume-Tilting
- 7 Flume Support by Truss-Structure

- 8 Flume Tilting Mechanism
- 9 Outlet / Settling Tank

Flow Directions:

- a Inlet Flow from Water Pump
- b Flow in Flume
- c Outlet Flow

b)

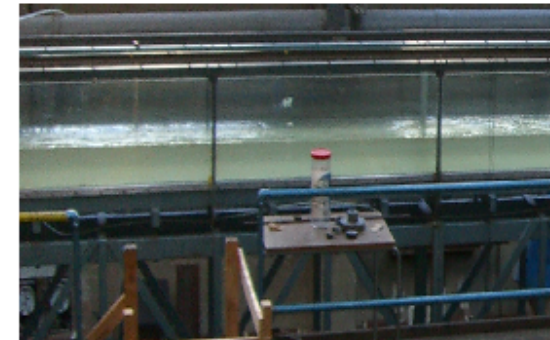


Figure 1. a) Sketch layout of the experimental flume with dimensions of 12m (length) \times 0.45m (width) \times 0.50m (height) (the layout is not drawn in proportion to the actual dimensions), and b) photograph of a test section of the flume.

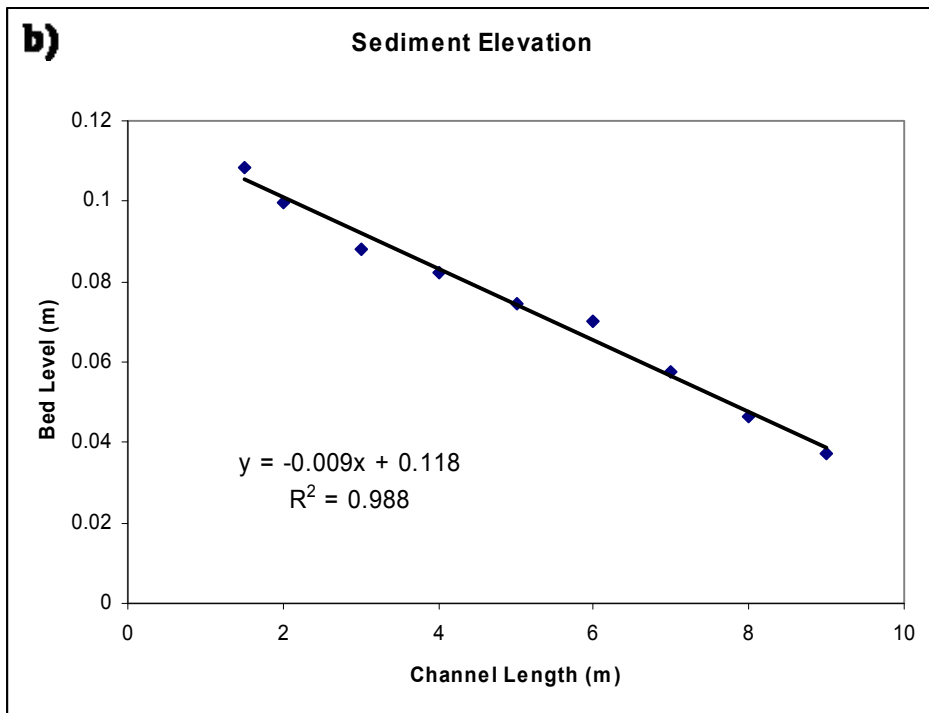
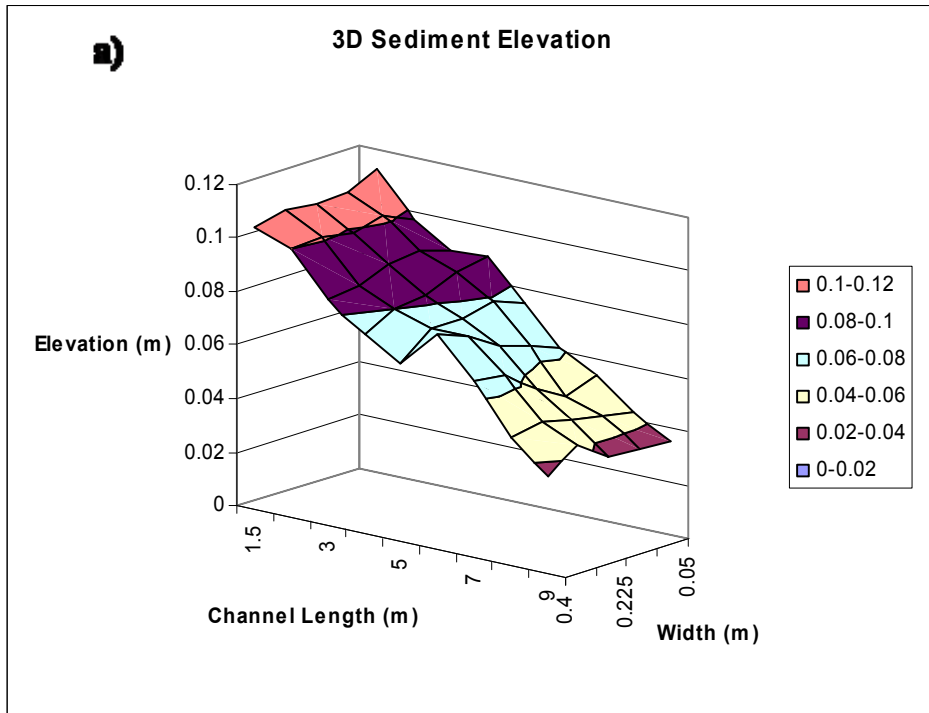


Figure 2. a) 3D sediment elevation profile in flume, and b) sediment bed elevation (averaged through the channel width) measured after the bed feeding



Figure 3. Bed material sample used in the experiment

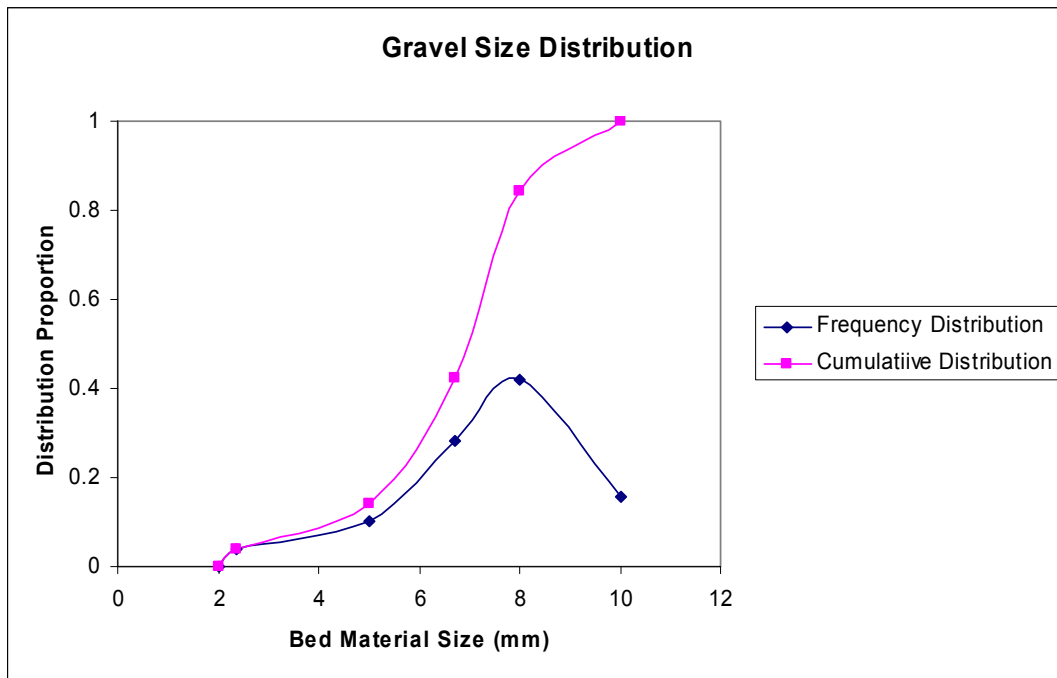


Figure 4. Cumulative and frequency distributions of the bed material size

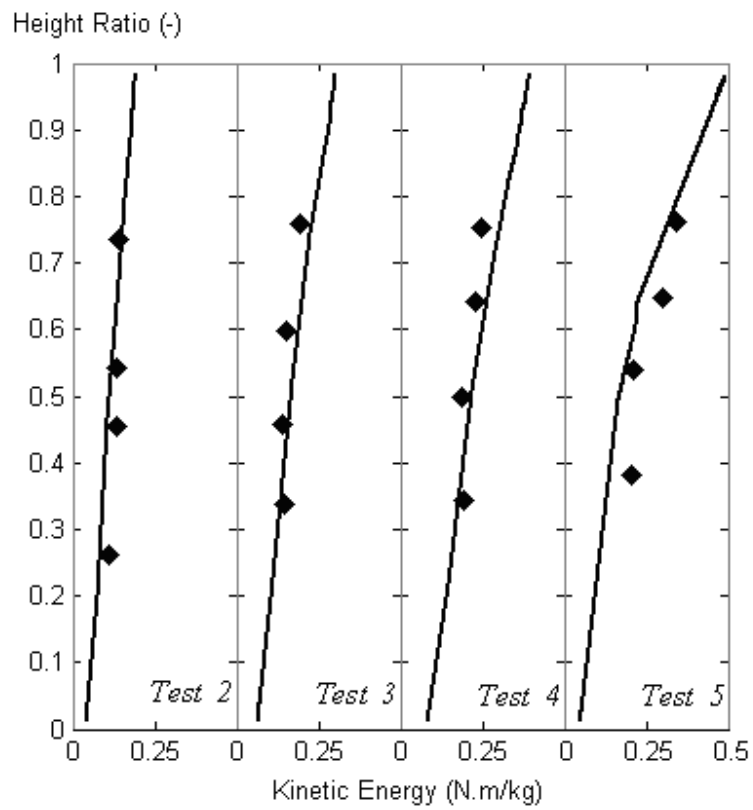


Figure 5. Non-uniform flows depth-averaged TKEs against the water height ratio h_{dr} (symbol – experiment, line – numerical simulation)

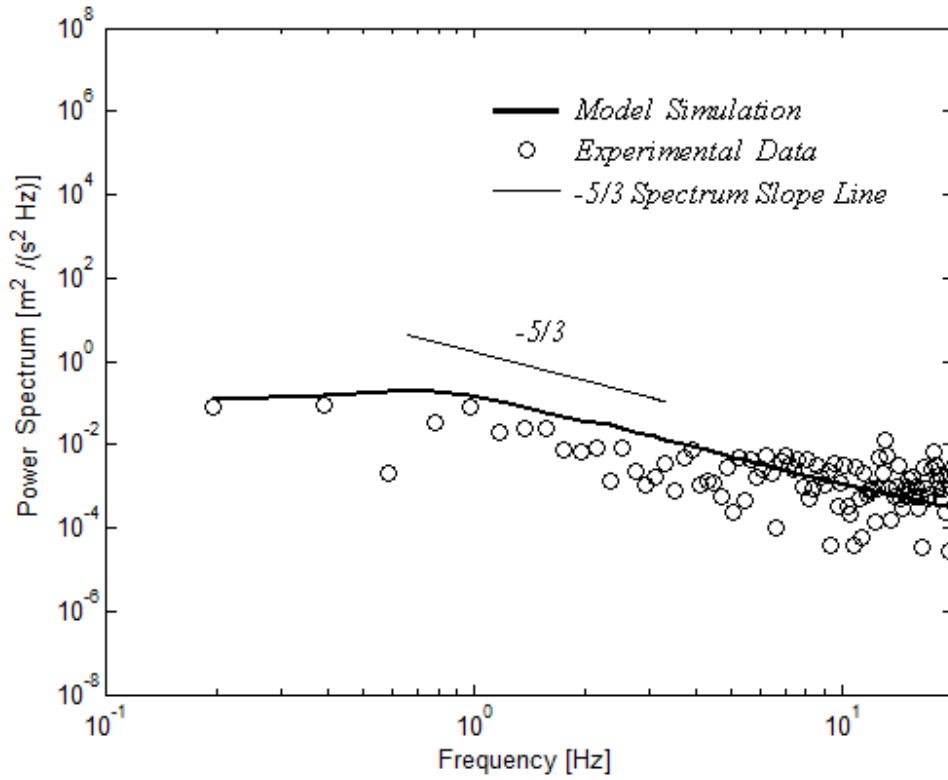


Figure 6. Power spectrum of Test 1 at 6m streamwise location of the channel (symbol – experimental measurement, thick line – numerical simulation, thin line – K41 scaling rule)

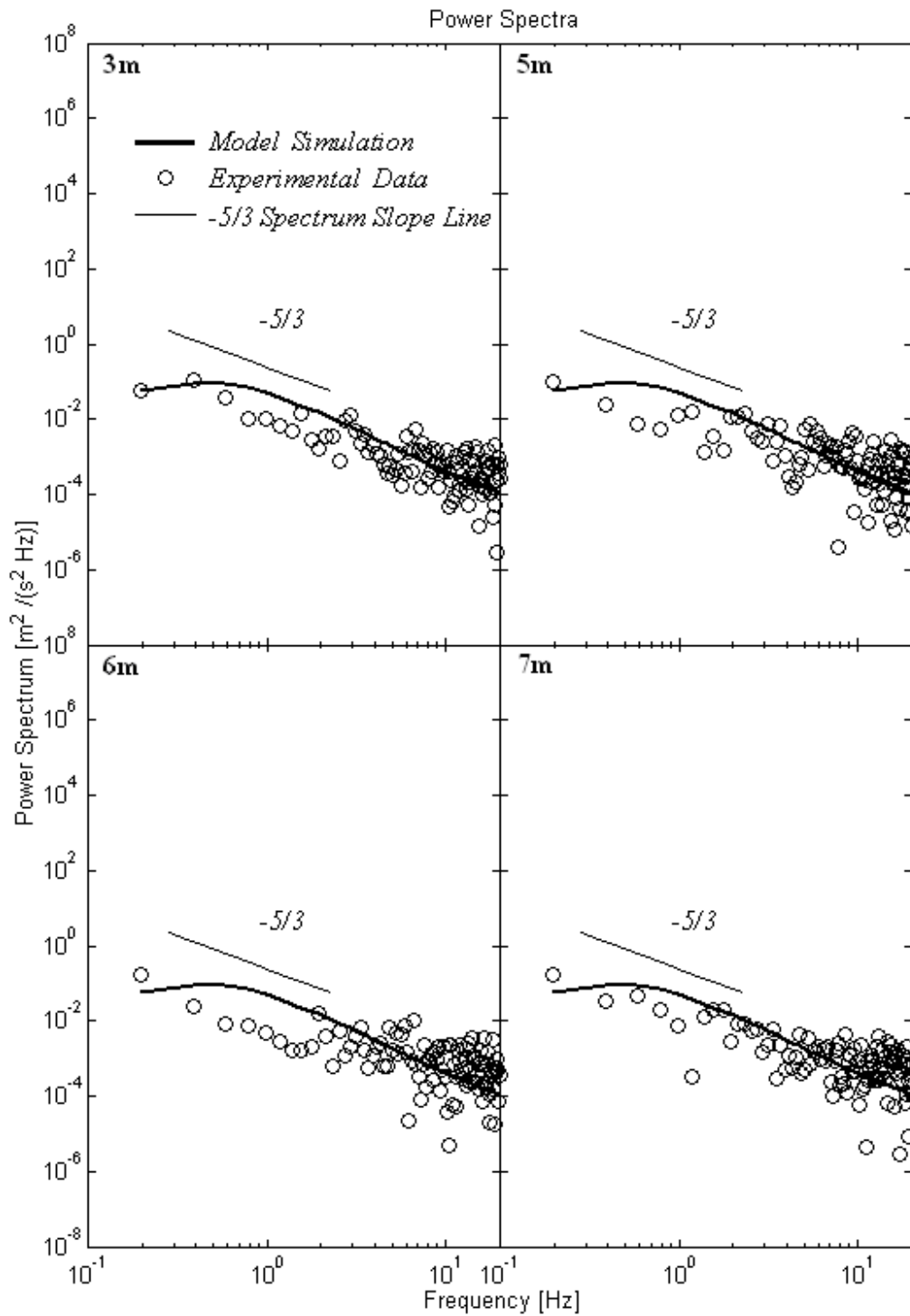


Figure 7. Power spectra of Test 2 at different streamwise locations of the channel (symbol – experimental measurement, thick line – numerical simulation, thin line – K41 scaling rule)

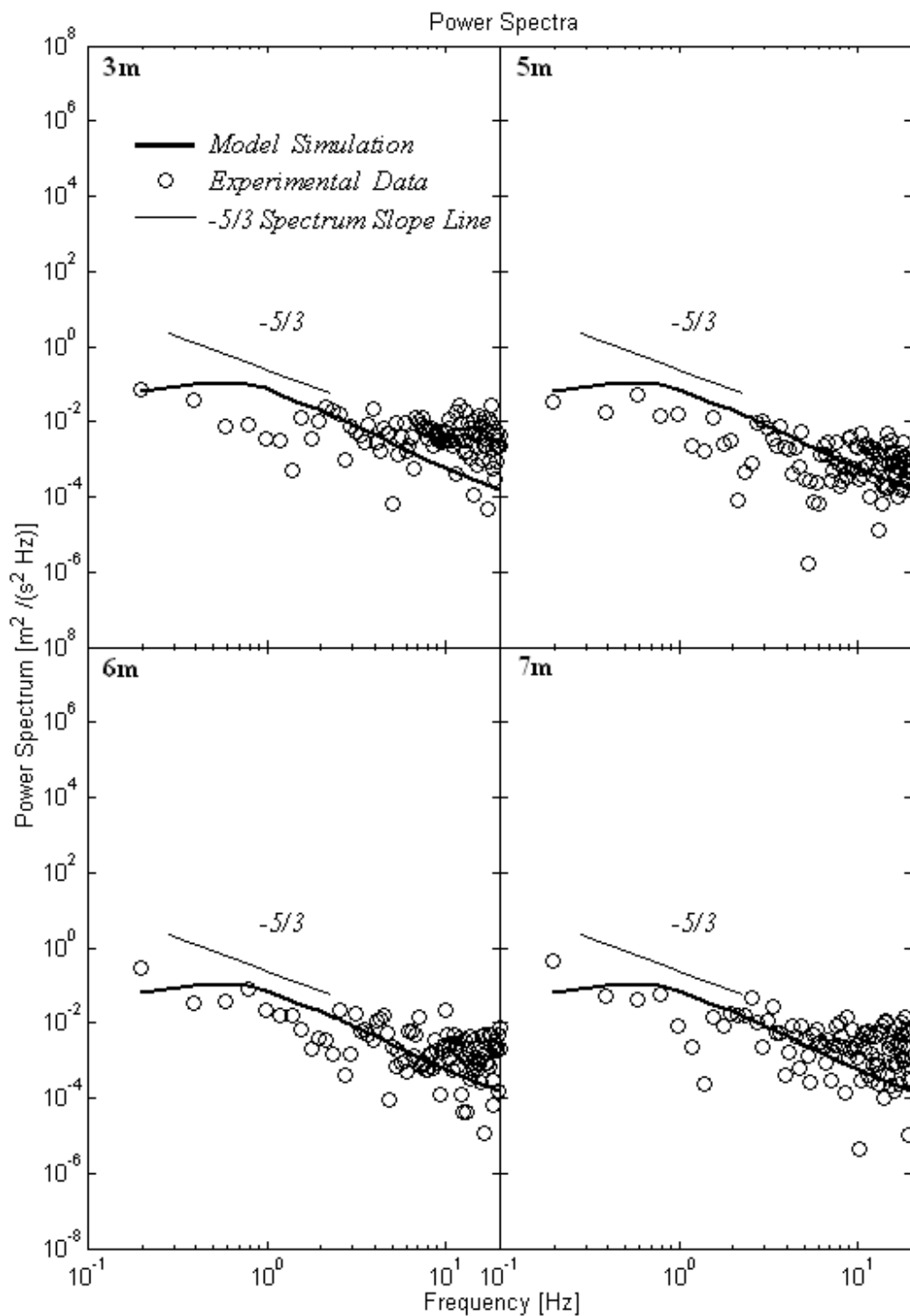


Figure 8. Power spectra of Test 3 at different streamwise locations of the channel (symbol – experimental measurement, thick line – numerical simulation, thin line – K41 scaling rule)

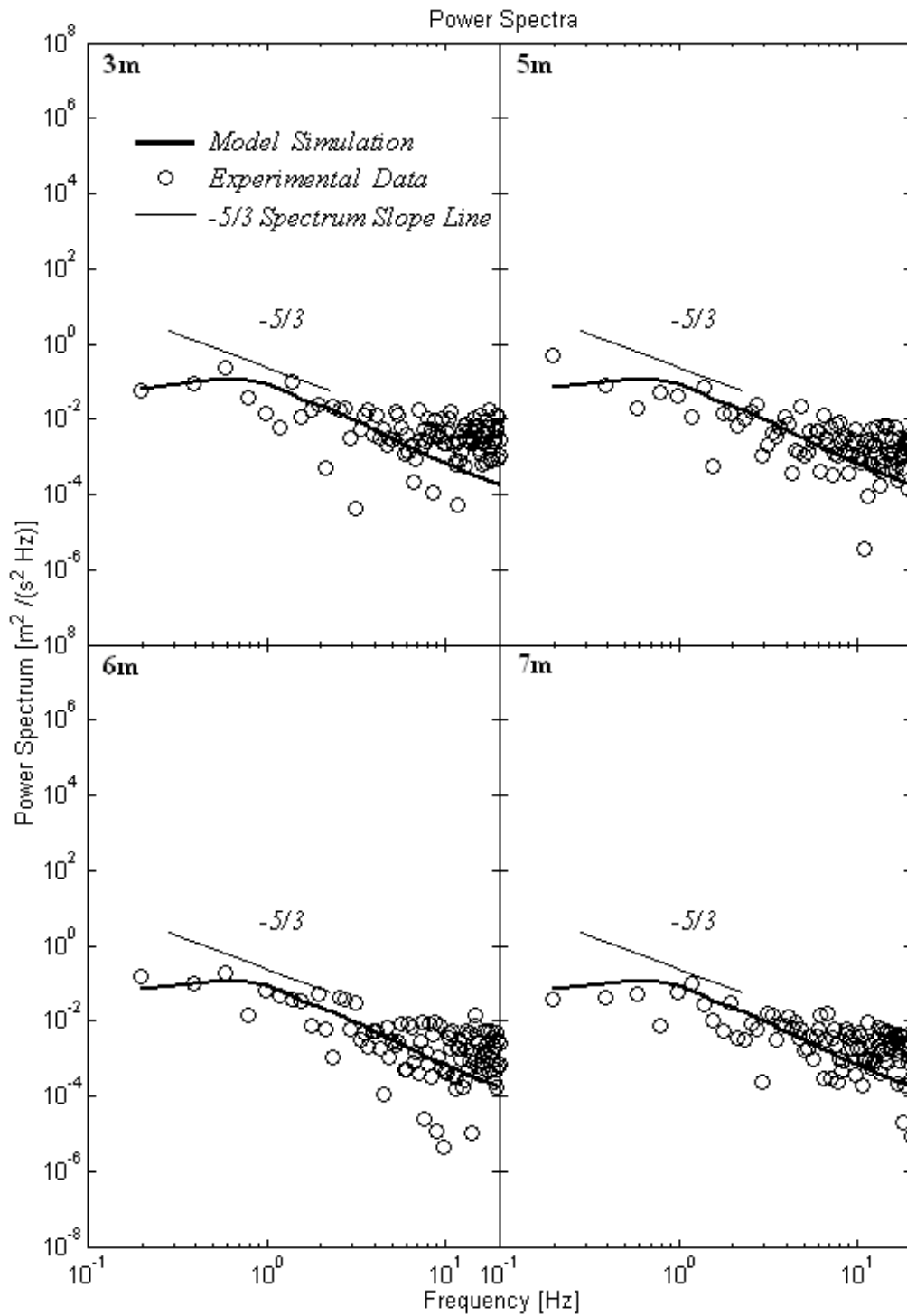


Figure 9. Power spectra of Test 4 at different streamwise locations of the channel (symbol – experimental measurement, thick line – numerical simulation, thin line – K41 scaling rule)

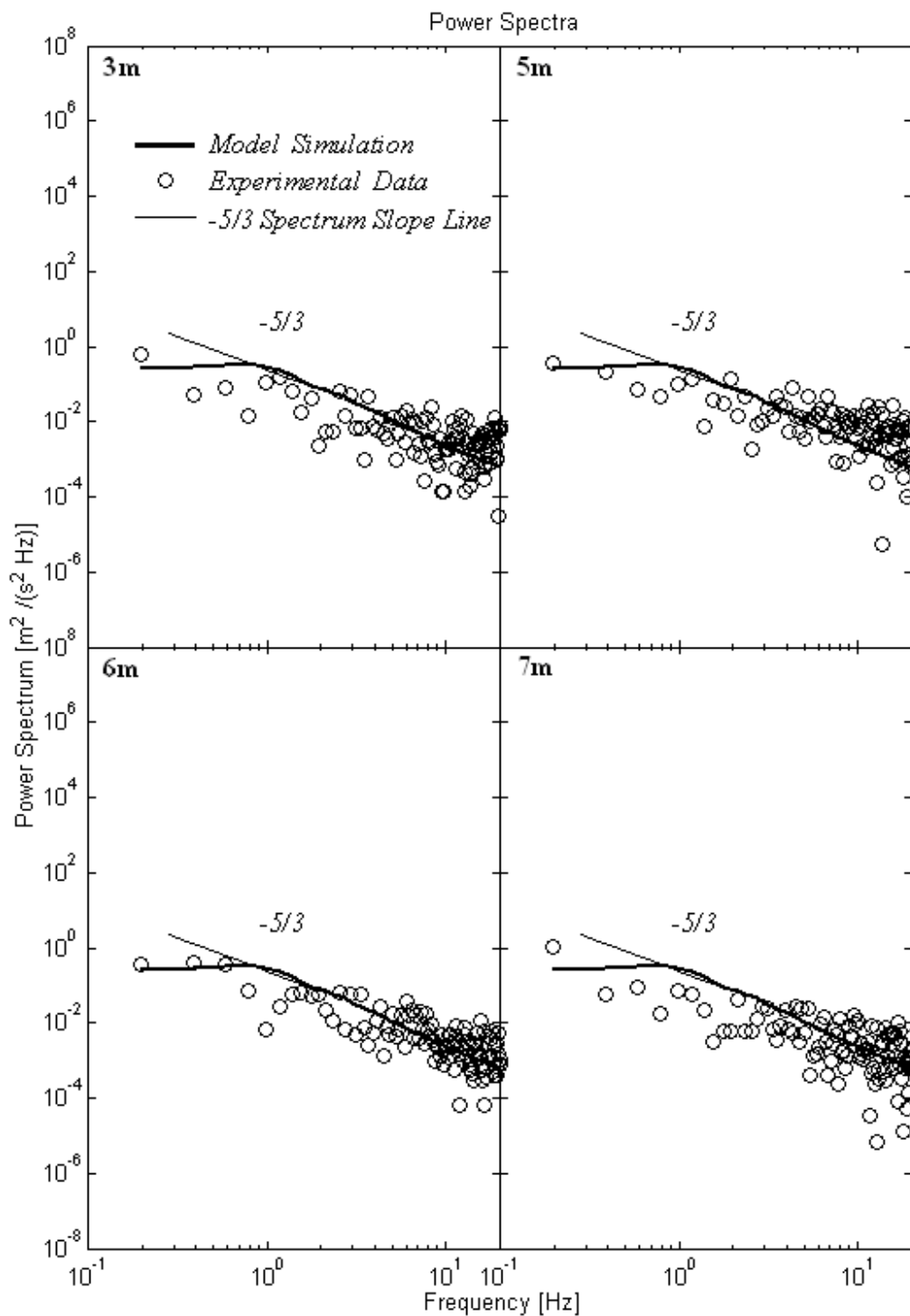


Figure 10. Power spectra of Test 5 at different streamwise locations of the channel (symbol – experimental measurement, thick line – numerical simulation, thin line – K41 scaling rule)

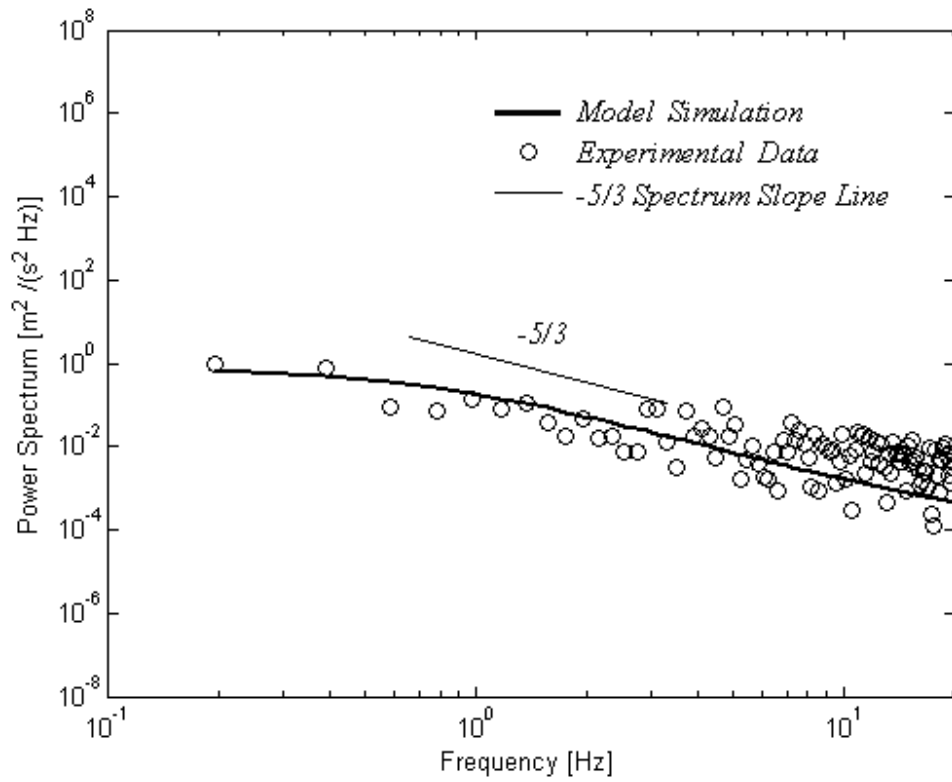


Figure 11. Power spectrum of Test 6 at 6m streamwise location of the channel (symbol – experimental measurement, thick line – numerical simulation, thin line – K41 scaling rule)